Cationic pair substitution in $LaAlO_3:Mn^{4+}$ for octahedral-tilting dependent zero-phonon line

Siyuan Li,[a] Chenyu Zhang,[a] Qi Zhu[*a] and Ji-Guang Li[*b]

[a]*Key Laboratory for Anisotropy and Texture of Materials (Ministry of Education), School of Materials Science and Engineering, Northeastern University, Shenyang, Liaoning 110819, China*

[b]*Research Center for Functional Materials, National Institute for Materials Science, Namiki 1-1, Tsukuba, Ibaraki 305-0044, Japan*

*Corresponding authors:

Dr. Qi Zhu

Tel: +86-24-8367-2700

E-mail: zhuq@smm.neu.edu.cn

Dr. Ji-Guang Li

Tel: +81-29-860-4394

E-mail: LI.Jiguang@nims.go.jp

Abstract

Zero-phonon line (ZPL) emission of Mn^{4+}, without participation of phonon, is tightly related to the host crystal structure. However, the intensity of the intrinsic ZPL is much weaker than that of Stokes and anti-Stokes vibrational bands, and it always leads to a discontinuous emission peak. Regulating ZPL of Mn^{4+} for a charming emission is very important but remains a challenge for perovskite type oxides. Here, novel $La_{1-x}Ba_xAl_{1-x}Ti_xO_3$:0.001$Mn^{4+}$ (LBAT:0.001Mn^{4+}, x=0-0.2) and $La_{1-y}Y_yAl_{1-y}Ga_yO_3$:0.001$Mn^{4+}$ (LYAG:0.001Mn^{4+}, y=0-0.2) samples were successfully synthesized through a high-temperature solid-state reaction, and tunable ZPL of Mn^{4+} was found by cationic pair substitution of Ba^{2+}-Ti^{4+} and Y^{3+}-Ga^{3+} for La^{3+}-Al^{3+} in $LaAlO_3$:Mn^{4+}. The ZPL intensity is related to the local symmetry around Mn^{4+} and the ZPL energy corresponds to the Mn-O bond distance and the O-Mn-O bond distortion. Through co-doping Ba^{2+}-Ti^{4+}, the ZPL at 710 nm is enhanced and the intensity increases continuously with increasing the x value, due to the local symmetric degree of Mn^{4+} decreases slowly. However, the Y^{3+}-Ga^{3+} co-doping induces linear and quick increase of the intensity of ZPL at 704 nm with increasing y value, due to the local symmetric degree of Mn^{4+} decreases quickly. The octahedral tilting distortion is very important for the local symmetry. Ba^{2+}-Ti^{4+} co-doping reduces octahedral tilting distortion, but Y^{3+}-Ga^{3+} co-doping induces a serious octahedral tilting distortion. Consequently, the ZPL emission exhibits an octahedral-tilting dependent behavior. Mainly due to the larger distortion of O-Mn-O bond, the energy of ZPL for LYAG:0.001Mn^{4+} is higher than that for LBAT:0.001Mn^{4+}. The outcomes of this work

provide a promising way to regulate the ZPL intensity and energy by tuning the local structure around Mn^{4+}, and they may have wide implication for Mn^{4+}-doped phosphors and solid state lighting.

1. Introduction

The ABO_3 perovskite oxides present a multitude of functional properties and are widely renowned for their potential in various types of applications, owing to their low cost and high abundance.[1,2] For the simple ABO_3 perovskite, A cation connects to 12 oxygen atoms to form a AO_{12} dodecahedron, and B cation links with 6 oxygen atoms to form a BO_6 octahedron. BO_6 is connected each other by O vertices to form the three-dimensional framework structure, and A cations are located in the cavities surrounded by eight BO_6 octahedra.[3,4] The most common distortion for ABO_3 perovskite oxide is octahedral tilting, which is related to the rigid BO_6 rations while keeping their corner-sharing connectivity.[5,6] Controlling the degree of octahedral tilting is of great interest, owing to its significant effects on the physical and chemical properties.

$LaAlO_3$ has rhombohedral symmetry with a pseudo-cubic cell parameters $a=b=c$=3.79 Å and β=90.066°, and it is one of the most important ABO_3 perovskite oxides.[7,8] It is widely known that the phase transition from cubic to rhombohedral takes place at T_c ~817 K through AlO_6 octahedron rotating along <-11-1> with half of the polyhedrons tilting clockwise and half tilting anticlockwise.[9] During the rotation, the local structure changes a lot, which can be determined by the analysis of cell

parameter variation and Raman spectra. Furthermore, the structural changes from rhombohedral to cubic with increasing hydrostatic pressure are also observed, which are induced by decreasing AlO_6 octahedron tilting.[10] Not only the temperature and pressure can alter the tilting degree of AlO_6, but also the replacement of La^{3+} or/and Al^{3+} by other cations.[11,12] For example, when Nd^{3+} cations substitute La^{3+} in $LaAlO_3$, the AlO_6 octahedron tilting increases gradually.[11] The octahedron tilting distortions would induce huge variations for local structure and produce an impact on properties of the functional materials.[7]

$LaAlO_3$ is an appropriate host for Mn^{4+} doping to generate near-infrared emission.[12] Mn^{4+} with $3d^3$ electronic configuration is an excellent luminescent center.[13,14] Usually, Mn^{4+} prefer to occupy the octahedral sites to generate the luminescence, which depends on the covalence and local coordination symmetry around Mn^{4+} in the host. The emission peak of Mn^{4+} corresponded to ^2E_g-$^4A_{2g}$ usually consists of the zero-phonon line (ZPL) transition and the vibrational sidebands of ZPL with phonon assistance (Stokes and anti-Stokes vibronic band) ranging from 600-800 nm.[15] Compared with phonon sidebands, the energy and intensity of ZPL are much more sensitive to the local coordinated environment. The reason is that any phonon does not participate in the ZPL emission process, which is only dependent on the host structure.[16,17] Generally, the intensity of ZPL is related to the structure symmetry around Mn^{4+}. According to the Tanabe-Sugano diagram, the ZPL emission energy remains the same with changing the crystal field splitting. In fact, the energy of Mn^{4+} emission is based on Mn-ligand hybridization.[18,19] Decreasing hybridization should

lead to higher ^2E_g energies and increase the emission energy. Furthermore, weaker hybridization can be induced via the increased Mn-ligand distance and/or distorted ligand-Mn-ligand bond angles.[18] Mn^{4+} doped phosphors are usually used as the red component in LED devices. Interestingly, when the ZPL is located at the wavelength smaller than 700 nm, the color rendering index of LED devices can be further improved with enhancing the ZPL emission, which is very important to obtain the high-quality white LED devices.[14] Because ZPL of the $LaAlO_3:Mn^{4+}$ phosphor is located at the wavelength larger than 700 nm, enhancing ZPL can not improve the color rendering index of the white LED device. However, the $LaAlO_3:Mn^{4+}$ phosphors can be used as LED devices, which are benefit for plant growing.[13] At the same time, higher ZPL intensity can induce the divided two emission peaks (Stokes and anti-Stokes) become a broad band, and then make the emission spectra better match with the P_{FR} region of plant absorption spectrum. Consequently, the luminous efficiency of phosphor with continued and broad emission band is higher than the phosphor with divided emission band.[12] Therefore, exploring the changes of ZPL energy and intensity along with the local structure is vital for designing high efficiency deep-red or near-infrared phosphors.

In our previous work,[12] zero-phonon line (ZPL) emission of Mn^{4+} was generated by substituting Mg^{2+}-$Ge^{4+}$for Al^{3+}-Al^{3+} in $LaAlO_3:Mn^{4+}$, which resulted in a significant octahedral tilting distortion and a mismatched cation size distortion. The local structure of Mn^{4+} is influenced by MgO_6 and GeO_6, which link to MnO_6 through O vertex. In this way, the symmetry degree of Mn^{4+} decreases gradually along with

increasing Mg^{2+}-Ge^{4+} content, which induce an improvement of ZPL emission. However, the energy of ZPL emission is not discussed in detail in previous work, due to insufficient impact on the local structure around Mn^{4+}. In order to further reveal the relationship between the local coordinated environment around Mn^{4+} and the ZPL behavior (energy and intensity), a cationic pair substitution way to tune the local structure was proposed here through replacing La^{3+}-Al^{3+} rather than Al^{3+}-Al^{3+} by Ba^{2+}-Ti^{4+} and Y^{3+}-Ga^{3+} in $LaAlO_3$:0.001Mn^{4+}. BaO_{12} and YO_{12} polyhedrons connect with MnO_6 by sharing the same plane and edge, and GaO_6 and TiO_6 octahedra link to MnO_6 through O vertex. So, they would show more serious effect on local structure of Mn^{4+}, comparing to that only sharing the same O vertex by Mg^{2+}-Ge^{4+} substitution for Al^{3+}-Al^{3+}. Thus, in this work, $La_{1-x}Ba_xAl_{1-x}Ti_xO_3$:0.001$Mn^{4+}$ (LBAT:0.001Mn^{4+}, x=0-0.2) and $La_{1-y}Y_yAl_{1-y}Ga_yO_3$:0.001$Mn^{4+}$ (LYAG:0.001Mn^{4+}, y=0-0.2) samples were successfully synthesized through the high-temperature solid-state reaction in atmospheric environment. The variations of the local structure were detected by the XRD Rietveld refinement, Raman spectra, SEM and TEM analysis. The luminescence properties were obtained by the diffuse reflectance spectra, PLE spectra, PL spectra, lifetime decay curves and temperature-dependent PL spectra. Through above analysis, the relationship between the local structure of Mn^{4+} and ZPL behavior (energy and intensity) was discussed in detail.

2. Experimental section

Sample preparation

A series of $La_{1-x}Ba_xAl_{1-x}Ti_xO_3$:0.001$Mn^{4+}$ (LBAT:0.001Mn^{4+}, x=0-0.25) and $La_{1-y}Y_yAl_{1-y}Ga_yO_3$:0.001$Mn^{4+}$ (LYAG:0.001Mn^{4+}, y=0-0.25) samples were

synthesized by the traditional high-temperature solid-phase reaction technique. La_2O_3, Al_2O_3, $MnCO_3$, $BaCO_3$, Y_2O_3, TiO_2 and Ga_2O_3 were used as raw materials. La_2O_3 (99.99%) and Y_2O_3 (99.999%) were purchased from Huizhou Ruier Rare-Chem. Hi-Tech. Co. Ltd (Huizhou, China). Al_2O_3 (99.99%), $MnCO_3$ (99.95%), $BaCO_3$ (99.99%), TiO_2 (99.8%), and Ga_2O_3 (99.99%) were purchased from Aladdin Chemical Reagent Co. Ltd (Shanghai, China). La_2O_3 was heated at 1000 ^oC for 2 h before use for removing adsorbed water. The raw materials were accurately weighed according to the stoichiometric molar ratio of the designed compositions. Then, these raw materials were placed in agate mortar and grinded for 30 min to be mixed thoroughly. After that, the mixtures were preheated at 1000 ^oC for 5 h and then sintered at 1500 ^oC for 8 h in air. The final powders were obtained to further measurement after cooling down to room temperature naturally.

Characterization methods

The phase compositions of the samples were obtained by X-ray powder diffraction (XRD, Model SmartLab, Rigaku, Tokyo, Japan) with the use of nickel-filtered Cu Kα radiation (λ=0.15406 nm) and 40 kV, 200 mA operating conditions. The scanning range was 10-90 ^{o} and the scanning rate was 6 ^{o} per minute. The XRD patterns for Rietveld refinement were acquired in the range of 10-110^o at a step size of 0.02 ^{o} with a step-scan mode of 2.5 s per step. The product morphology, microstructure and element mapping were analyzed through field emission scanning electron microscopy (FE-SEM, Model JSM-7001F, JEOL, Tokyo) and transmission electron microscopy (TEM, Model JEM-2000FX, JEOL, Tokyo). Raman spectra were collected via a Raman microscope (Model R-XploRA Plus, Horiba, Paris, France)

with the use of a 638 nm laser. The diffuse reflectance spectra were conducted with a Model UV-3600 Plus instrument (Shimadzu, Kyoto, Japan). Photoluminescence and fluorescence decays of the phosphors were recorded on a FP-8600 fluorospectrophotometer (JSACO, Tokyo) with a temperature controller (HPC-836, JSACO) and a liquid nitrogen cooling unit (PMU-830, JSACO). The internal quantum yield (IQY) of the samples were measured using the integrated sphere on the same FP-8600 instrument.

3. Results and discussion

3.1 Crystal structure and microstructure

Fig. 1a shows a detailed crystal structure of $LaAlO_3$ and the coordination environment of the cations. AlO_6 octahedra are connected with each other by corner-sharing to form the basic framework of $LaAlO_3$. The La^{3+} ion is coordinated with twelve oxygen atoms and located in the cavities of eight AlO_6 octahedra. According to the similar ionic radii between Mn^{4+} (0.53 Å, CN=6) and Al^{3+} (0.535 Å, CN=6), the luminescence centers Mn^{4+} ions would occupy the crystallographic sites of Al^{3+} in AlO_6 units. Therefore, from the consideration of ionic radii, Ti^{4+} (0.605 Å, CN=6) and Ga^{3+} (0.62 Å, CN=6) are expected to substitute Al^{3+} (0.535 Å, CN=6). Moreover, Ba^{2+} (1.61 Å, CN=12) and Y^{3+} (1.075 Å, CN=9) would replace La^{3+} (1.36 Å, CN=12). Figs. 1b and 1c show the XRD patterns of the LBAT:0.001Mn^{4+} (x=0-0.25) and LYAG:0.001Mn^{4+} (y=0-0.25) samples. Obviously, most of the samples fit well with the standard crystal diffraction data (JCPDS No. 85-0848) of $LaAlO_3$ compound. However, when the x value and y value exceed 0.2, the impurity of

$BaTiO_3$ (JCPDS No. 75-2117)[20] and $Y_4Al_2O_9$ (JCPDS No. 83-0935)[21] are yielded, respectively. Therefore, later discussion is based on the *x* value and *y* value no more than 0.2. As it is seen in Figs. 1b and 1c, all the diffraction peaks shift to lower angles gradually with increasing *x* and *y* values. To analyze the shifts of diffraction peak with increasing *x* and *y* values, enlarged XRD patterns in the range of 32-34° are shown in Figs. 1b and 1c. The strongest diffraction peak at 33.4° shifts toward lower angles with increasing *x* and/or *y* value. But, the LBAT:0.001Mn^{4+}(*x*=0-0.2) samples show a larger shift than that for LYAG:0.001Mn^{4+} (*y*=0-0.2) samples. Typically, the average ionic radii of Ba^{2+}-Ti^{4+} and Y^{3+}-Ga^{3+} pair are both larger than that of La^{3+}-Al^{3+} pair, and Ba^{2+}-Ti^{4+} is the largest among the three pairs. Modulating the Ba^{2+}-Ti^{4+} and Y^{3+}-Ga^{3+} content in $LaAlO_3$:0.001Mn^{4+} could lead to the lattice volume expansion, and the results were in accordance with the experimental data. The dopants entered the crystal structure of $LaAlO_3$:0.001Mn^{4+} successfully, and the homogeneous solid solutions were formed. In addition, the diffraction peaks broaden evidently with increasing *x* and/or *y* value from 0 to 0.2, demonstrating the crystal lattice becomes imperfect and the distortion degree of the crystal structures increases.[22]

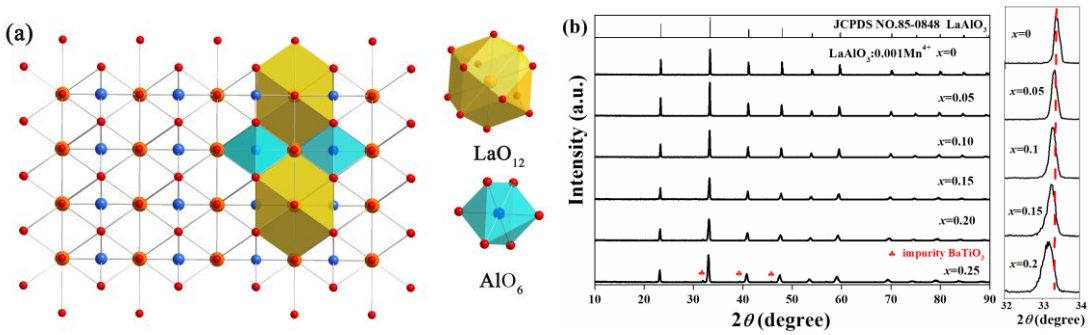

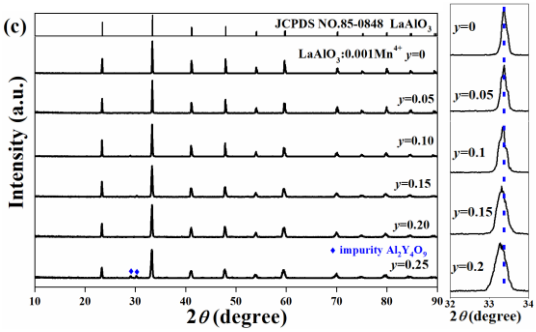

Fig. 1 (a) Crystal structure of $LaAlO_3$. XRD patterns of (b) LBAT:0.001Mn^{4+} (x=0-0.25) and (c) LYAG:0.001Mn^{4+} (y=0-0.25) in 2θ range of 10-90^o and enlarged XRD patterns in range of 32-34^o.

In order to further observe the variation of the crystal lattice of $LaAlO_3$:0.001Mn^{4+} after incorporation of Ba^{2+}-Ti^{4+} and Y^{3+}-Ga^{3+} pairs, the Rietveld refinements were conducted (Fig. S1). The refinement results for LBAT:0.001Mn^{4+} (x=0-0.2) and LYAG:0.001Mn^{4+} (y=0-0.2) samples were summarized in Tables S1 and S2, respectively. As can be seen, the residual factors (R_{wp}, R_p and χ^2) for all the samples converged to low levels, showing that these refinement results are reliable. The lattice constant and the M-O bond length in MO_6 octahedra increase linearly with increasing the doping content of Ba^{2+}-Ti^{4+} and Y^{3+}-Ga^{3+} (Figs. 2a and 2b). The O-M-O bond angle shows a decreasing trend with the increase of x value, while it shows a remarkably increasing trend with increasing y value (Fig. 2c). The octahedral tilting can be reflected by the octahedral tilting angle φ between the Al-O bonding and the coordinated axis, which is the angle deviated 90.00^o.[7] The increased φ value shows serious octahedral tilting distortion with Y^{3+}-Ga^{3+} co-doping, but the value decreases with increasing x value, implying that the octahedral tilting distortion is suppressed (Fig. 2d). These variations of the samples co-doped Ba^{2+}-Ti^{4+} and Y^{3+}-Ga^{3+} in lattice constant, bond length, bond angle and tilting angle are different from each other, implying that co-doping Ba^{2+}-Ti^{4+} and Y^{3+}-Ga^{3+} pairs may result in

various distortions of the crystal lattice, owing to the mismatch in ionic radii of doping cations and the resultant octahedral tilting degrees.[23,24] Consequently, the distortions of LBAT:0.001Mn^{4+}(x=0.05-0.2) samples are caused by the competition between the mismatched ionic radii and the suppression of octahedral tilting. On the contrary, the distortions of LYAG:0.001Mn^{4+} (x=0.05-0.2) are composed of the mismatched ionic radii and the increased octahedral tilting.

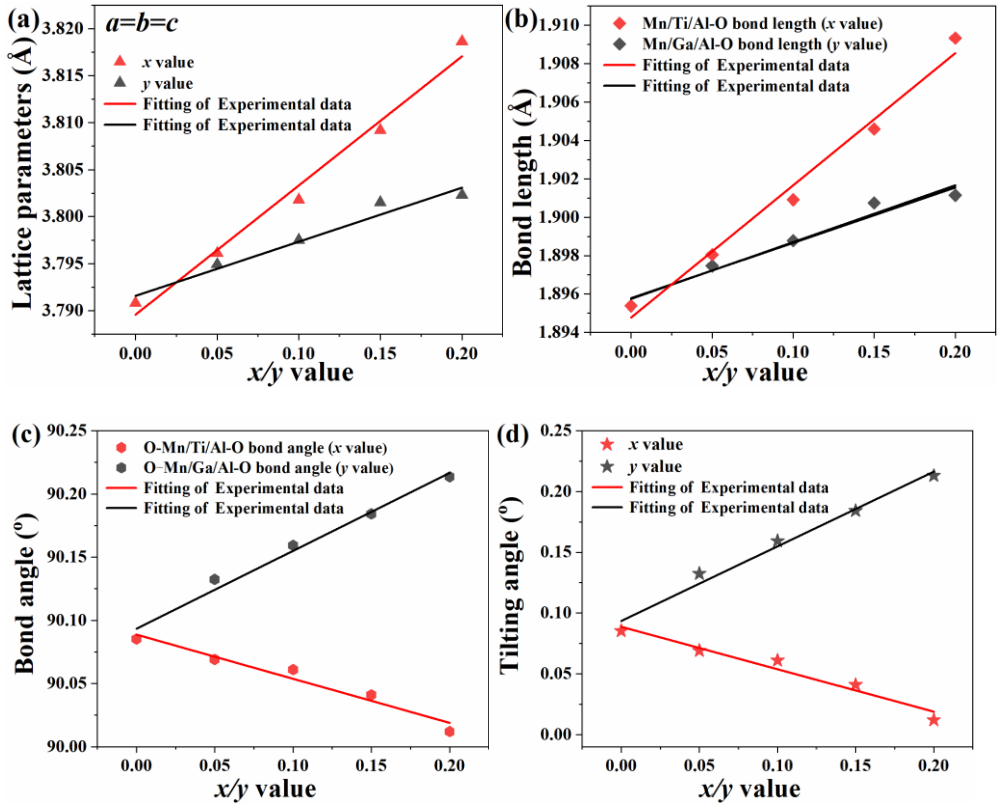

Fig. 2 The variations of (a) cell parameter, (b) bond length, (c) O-M-O bond angle in a MO_6 octahedron and (d) octahedral tilting angle versus various Ba^{2+}-Ti^{4+} (x=0-0.2) and Y^{3+}-Ga^{3+} (y=0-0.2) content doped $LaAlO_3$:0.001Mn^{4+} phosphors based on Rietveld refinement results.

Raman spectra is a useful tool to detect the distortion of $LaAlO_3$.[7,25] Figs. 3a and 3b display the Raman spectra of LBAT:0.001Mn^{4+} (x=0-0.2) samples and LYAG:0.001Mn^{4+} (y=0-0.2) samples, respectively. For $LaAlO_3$:0.001Mn^{4+} phosphor, two strong peaks at 121 and 152 cm^{-1} are observed, which are assigned to A_{1g} mode

(rotation of the oxygen octahedra) and E_g mode (pure La vibration), respectively. The wavenumber of A_{1g} mode mainly correlates with the tilting angle of AlO_6 octahedron.[11] A blue shift of the A_{1g} wavenumber from 121 to 109 cm^{-1} is detected with increasing the *x* value from 0 to 0.2, while a red shift from 121 to 195 cm^{-1} is observed with increasing the *y* value from 0 to 0.2. These phenomena explain that introducing Ba^{2+}-Ti^{4+} reduces the octahedral tilting, while co-doping Y^{3+}-Ga^{3+} pair increases the octahedral tilting. The results are consistent with the variations of tilting angle φ (Fig. 2d). At the same time, the E_g wavenumber at 152 cm^{-1} keeps in the same position with increasing the *x* or *y* value. Because the defects in the crystal structure may contribute to the broadening of the vibrational bands, the full width at half-maximum (FWHM) can reflect the amount of defects.[25] The FWHM value of the A_{1g} mode is 15 cm^{-1} for $LaAlO_3$:0.001Mn^{4+}, and the value shows a continuous increase with increasing the Ba^{2+}-Ti^{4+} and Y^{3+}-Ga^{3+} contents. Furthermore, the FWHM value of LYAG:0.001Mn^{4+} (*y*=0.05-2) is always higher than that LBAT:0.001Mn^{4+} (*x*=0.05-0.2), implying that introducing Y^{3+}-Ga^{3+} would generate more serious defects in the crystal structure.

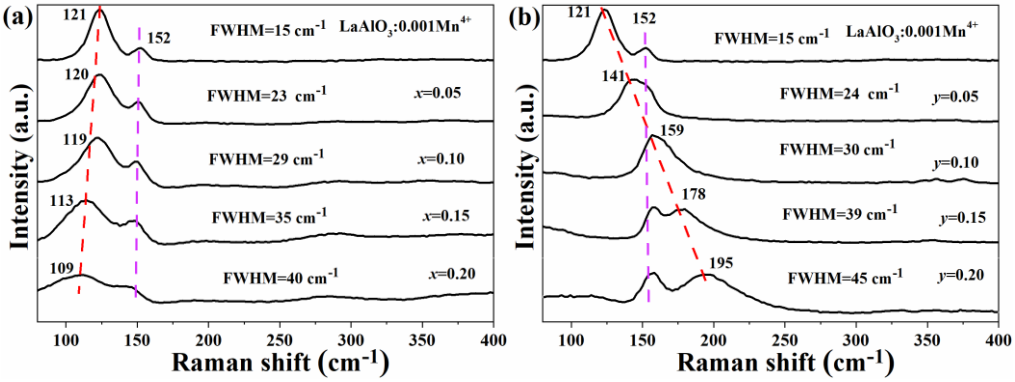

Fig. 3 Raman spectra of (a) LBAT:0.001Mn^{4+} (*x*=0-0.20) and (b) LYAG:0.001Mn^{4+} (*y*=0-0.20).

The SEM images, TEM images, HR-TEM lattice fringes and element distributions for $LaAlO_3$:0.001Mn^{4+}, x=0.2 and y=0.2 samples are displayed in Fig. 4. The particles are irregular in shape and the sizes are in the range of 1.5-6 μm, which are similar to the particles prepared at higher sintering temperatures.[26,27] Their surface morphology does not change significantly depending on the different co-doping amounts. The distinct interplanar space fingers indicate high crystallinity of the samples. The *d* values correspondent to (100) and (011) planes are determined to be ~0.377 and ~0.264 nm for $LaAlO_3$:0.001Mn^{4+} (Fig. 4c). The *d* value correspondent to (100) plane is calculated to be ~0.383 nm for x=0.2 sample, and the *d* value correspondent to (011) plane is estimated to be ~0.270 nm for y=0.2 sample. Due to the Ba^{2+}-Ti^{4+} and Y^{3+}-Ga^{3+} doping contribution to lattice expansion, an increase of the interplanar spacing is found with increasing the x and y value. The element mapping of a single particle indicates a uniform distribution of La, Al, O, Mn, Ba and Ti (Y and Ga) for x=0.2 (y=0.2) sample (Figs. 4g and 4k). After the comparative analysis, the optimal phosphor samples LBAT:0.001Mn^{4+} and LYAG:0.001Mn^{4+} were successfully synthesized.

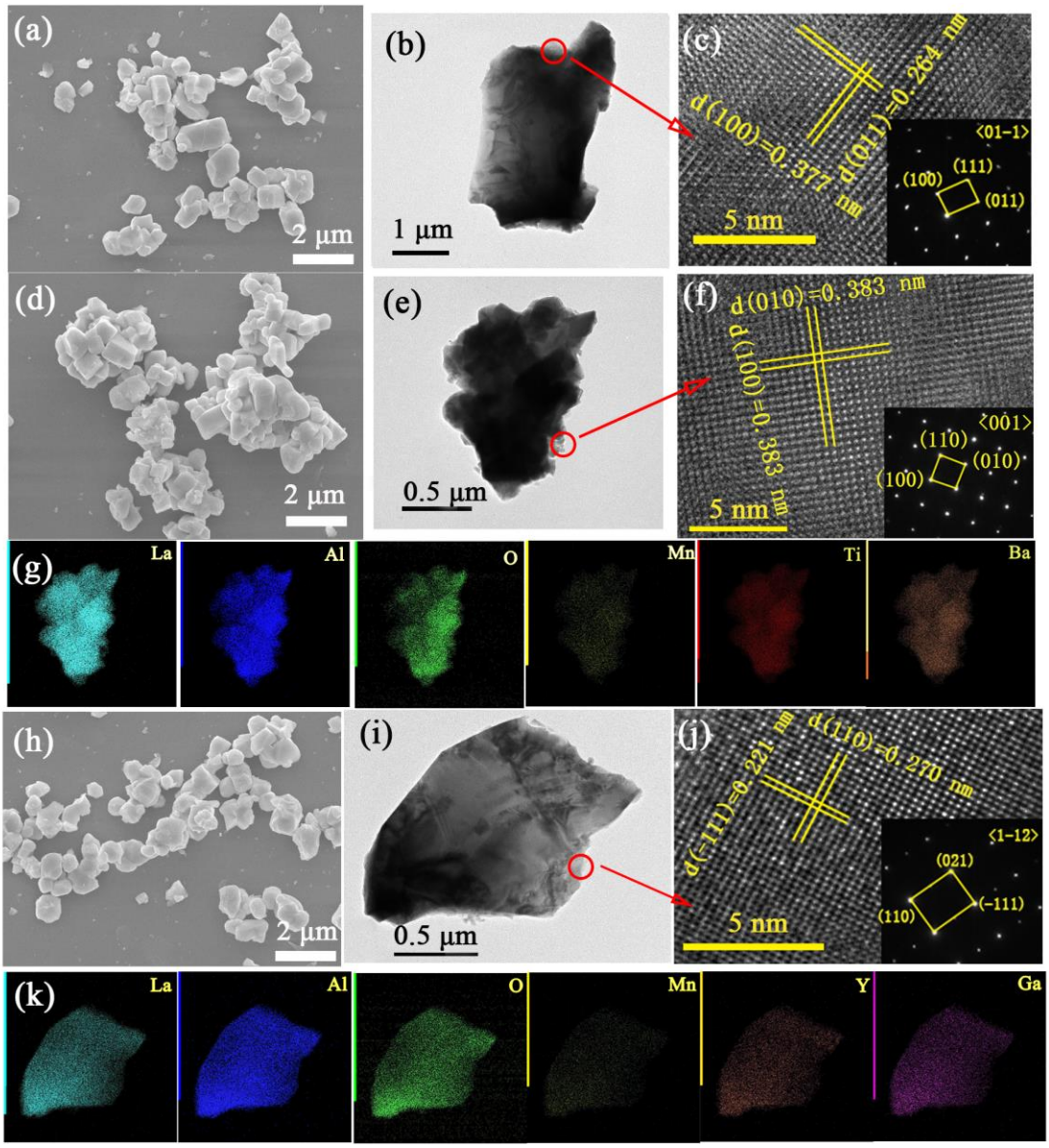

Fig. 4 SEM (a, d, h), TEM images (b, e, i), HR-TEM lattice fringes (c, f, j) and element distribution (g, k) for $LaAlO_3$:0.001Mn^{4+} (a, b, c), *x*=0.2 (d, e, f, g) and *y*=0.2 (h, i, g, k).

3.2 Photoluminescence of LBAT:0.001Mn^{4+} and LYAG:0.001Mn^{4+} samples

Fig. 5a reveals the diffuse reflection spectra of $LaAlO_3$:0.001Mn^{4+}, *x*=0.2 and *y*=0.2 samples. All the samples exhibit three strong and wide absorption bands from 240 to 550 nm, which correspond to the strong spin-allowed transition of Mn^{4+} from $^4A_{2g}$ to the excited levels $^4T_{1g}$, $^2T_{2g}$ and $^4T_{2g}$. But a strong band at ~280 nm related to the Mn^{4+}-O^{2-} charge-transfer band is only observed for $LaAlO_3$:0.001Mn^{4+} and

LYAG:0.001Mn^{4+} samples. For the purpose of gain more information about the band structures of above materials, the optical band gaps (E_g) were determined for $LaAlO_3$, $La_{0.8}Ba_{0.2}Al_{0.8}Ti_{0.2}O_3$ and $La_{0.8}Y_{0.2}Al_{0.8}Ga_{0.2}O_3$ hosts. The corresponding equation was used as follows:[28-30]

$$(\alpha h\nu)^n = A(h\nu - E_g) \qquad (1)$$

Where α, h, ν, and A represent the absorption coefficient, Planck constant, frequency and constant, respectively. n stands the direct or indirect transition while it is equal to 2 or ½, respectively. According to the previous report,[31] the band structure of $LaAlO_3$ is indirect. As shown in Fig. 5b, based on the plot of $(\alpha h\nu)^{1/2}$ vs $h\nu$, the E_g for $LaAlO_3$, $La_{0.8}Ba_{0.2}Al_{0.8}Ti_{0.2}O_3$ and $La_{0.8}Y_{0.2}Al_{0.8}Ga_{0.2}O_3$ is estimated to be 5.6, 3.9 and 5.7 eV, respectively. The Ba^{2+}-Ti^{4+} doping induces the large decrease of E_g value. For further analysis the changes of E_g, the band structure and the partial densities of states (DOS) for $La_{0.8}Ba_{0.2}Al_{0.8}Ti_{0.2}O_3$ were analyzed by density functional theory (DFT) calculation (Fig. S2). The band structure and DOS of $LaAlO_3$ were mentioned in our previous work, and the E_g value is 5.0 eV.[31] Furthermore, the La orbital levels dominantly contribute to the conduction band minimum (CBM), while the O orbital levels correspond to the valence band maximum (VBM). However, for the $La_{0.8}Ba_{0.2}Al_{0.8}Ti_{0.2}O_3$ host, the E_g value is 3.0 eV (Fig. S2a), which is much smaller than $LaAlO_3$. This is mainly due to that the electronic structure of CBM originates from Ti orbital levels predominantly, with the VBM still arising from the O orbital levels (Fig. S2b). It is noteworthy that there is a distinct smaller E_g of 3.0 eV for $La_{0.8}Ba_{0.2}Al_{0.8}Ti_{0.2}O_3$, confirming that Ba^{2+}-Ti^{4+} doping reduces the bandgap. The

results match well with the experimental data. Therefore, co-doping Ba^{2+}-Ti^{4+} in $LaAlO_3$ lead to the significant changes in E_g, and it may affect the luminescence properties of Mn^{4+}.

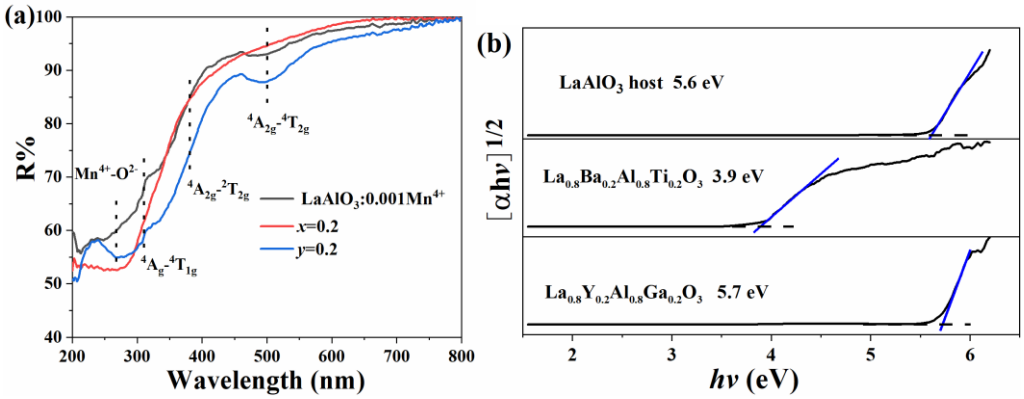

Fig. 5 (a) The diffuse reflection spectra of $LaAlO_3$:0.001Mn^{4+}, x=0.2 and y=0.2 samples. (b) The band gap energy determination for the selected hosts.

To investigate the effects of Ba^{2+}-Ti^{4+} and Y^{3+}-Ga^{3+} chemical unit doping on the luminescence of Mn^{4+}, the photoluminescence excitation (PLE) and photoluminescence (PL) spectra of LBAT:0.001Mn^{4+} (x=0-0.2) and LYAG:0.001Mn^{4+} (y=0-0.2) were measured and the results are shown in Fig. 6. There are two characteristic excitation bands appeared when monitored at 726 nm for $LaAlO_3$:0.001Mn^{4+}. The peak at 340 nm is assigned to the overlap of Mn^{4+}-O^{2-} charge-transfer band, $^4A_{2g}$-$^4T_{1g}$ and $^4A_{2g}$-$^2T_{2g}$ transitions, while the other peak at ~490 nm is related to the $^4A_{2g}$-$^4T_{2g}$ transition. There is an obvious red shift in the excitation spectra for LBAT:0.001Mn^{4+} (x=0-0.2) from ~333 to ~356 nm. The shift for LYAG:0.001Mn^{4+} (y=0-0.2) is from ~333 to ~358 nm. Furthermore, the peak at ~280 nm disappears for LBAT:0.001Mn^{4+} (x=0.05-0.2), while the PLE spectra of

LYAG:0.001Mn^{4+} (y=0.05-0.2) samples keeps the original shape. The appearance is due to the change of the optical band gap, which would be discussed in later. Under the 340 nm excitation, the PL spectrum of $LaAlO_3$:0.001Mn^{4+} is composed of two bands, including the anti-Stokes phonon band at 698 nm and Stoke phonon band at 726 nm of the ^2E_g-$^4A_{2g}$ transition. The zero-phonon line (ZPL) emission is too low in intensity to be detected. With the introduction of Ba^{2+}-Ti^{4+} and Y^{3+}-Ga^{3+}, both peaks keep at the same position and they persist the shape. However, a big difference between the anti-Stokes phonon band and the Stoke phonon band is found. A new peak at 710 or 704 nm was generated by co-doping Ba^{2+}-Ti^{4+} and Y^{3+}-Ga^{3+} in $LaAlO_3$:0.001Mn^{4+}, and, accordingly, the divided two peaks become a broad band. The new peak is related to the ZPL emission. Through the co-substitution of Ba^{2+}-Ti^{4+}, the new peak at 710 nm is enhanced slowly, while an unusual improvement of the peak at 704 nm is obtained by increasing Y^{3+}-Ga^{3+} content. Thus, due to the different ZPL energies and intensities, the PL shape of these phosphors shows a huge difference by co-doping different cation pairs.

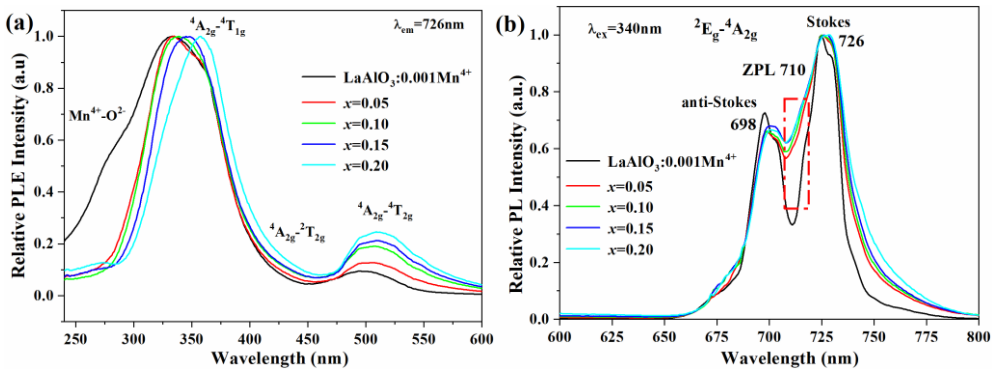

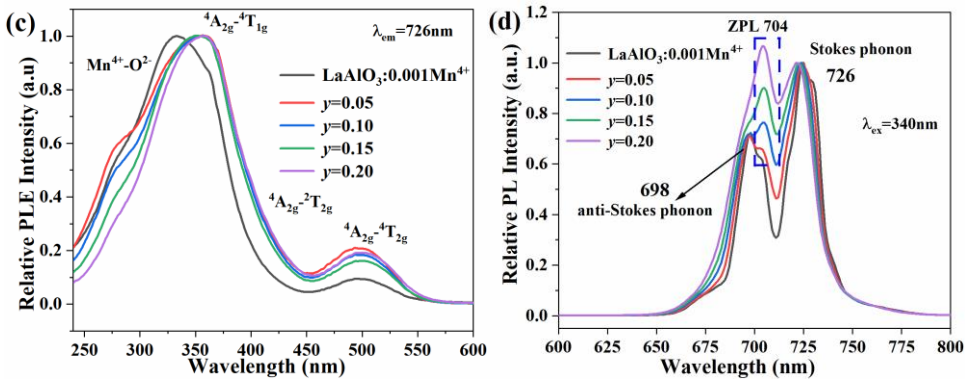

Fig. 6 PLE (a,c) and PL (b,d) spectra for (a,b) LBAT:0.001Mn^{4+} (x=0-0.2) and (c,d) LYAG:0.001Mn^{4+} (y=0-0.2) at room temperature.

As generally known, the emission of Mn^{4+} is mainly dominated by the vibration of the side bands. In order to observe the variations of ZPL in detail, the vibration of the side bands should be suppressed. Here, the high-resolution PLE and PL spectra of these samples were recorded at low temperature (77 K), as shown in Fig. 7. The excitation spectra are similar to the spectra measured at room temperature for the LBAT:0.001Mn^{4+} (x=0-0.2) and LYAG:0.001Mn^{4+} (y=0-0.2) samples. The PLE spectrum of $LaAlO_3$:0.001Mn^{4+} is fitted into four bands located at 316, 347, 410 and 490 nm, which are corresponding to the Mn^{4+}-O^{2-} charge-transfer band, $^4A_{2g}$-$^4T_{1g}$ and $^4A_{2g}$-$^2T_{2g}$ and $^4A_{2g}$-$^4T_{2g}$ transitions of Mn^{4+}. For the LBAT:0.001Mn^{4+} (x=0.05-0.2) phosphors, the PLE spectra can be well divided into three sub-bands, which are assigned to the $^4A_{2g}$-$^4T_{1g}$ and $^4A_{2g}$-$^2T_{2g}$ and $^4A_{2g}$-$^4T_{2g}$ transitions of Mn^{4+}. However, the PLE spectra of LYAG:0.001Mn^{4+} (y=0.05-0.2) phosphors are well-decomposed into four peaks, which are similar to $LaAlO_3$:0.001Mn^{4+} sample. Both $^4A_{2g}$-$^4T_{1g}$ and $^4A_{2g}$-$^4T_{2g}$ transition peaks show red shifts for LBAT:0.001Mn^{4+} (x=0-0.2) and LYAG:0.001Mn^{4+} (y=0-0.2) phosphors. Notably, under the excitation of 340 nm, the

Stokes peak is still at 726 nm and the anti-Stokes peak disappears at 77 K. According to the previous work, the red shift of Mn^{4+} excitation peaks is mainly due to the change of the crystal field strength (D_q). D_q could be estimated by the following equation:[16]

$$Dq = \frac{Ze^2r^4}{6R^5} \qquad (2)$$

Where Z stands the charge or valence of the anion, r and R represent the radius of the d wave function and the bond length between the Mn^{4+} and its ligands, respectively. In LBAT:0.001Mn^{4+} (x=0.05-0.2) and LYAG:0.001Mn^{4+} (y=0.05-0.2) phosphors, the average bond length of Mn-O is larger than that in $LaAlO_3$:0.001Mn^{4+} (Fig. 2b). Therefore, larger R can lead to a smaller D_q value, and it results in red shift of the excitation peak with increasing the x and y values. According to the Tanabe-Sugano energy level diagram, it can be seen that ^2E_g and $^4A_{2g}$ energy levels are almost parallel to horizontal ordinate.[12] Thus, ^2E_g and $^4A_{2g}$ energy levels are not affected by changing D_q, further implying that the emission energy is basically independent on the D_q.

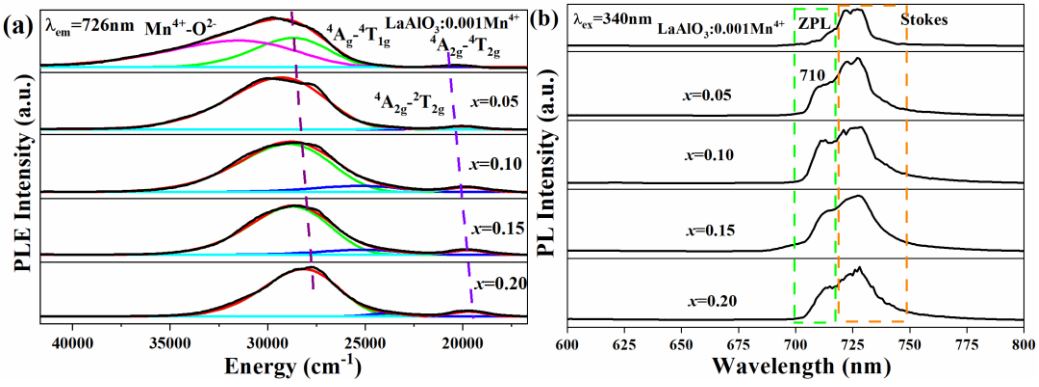

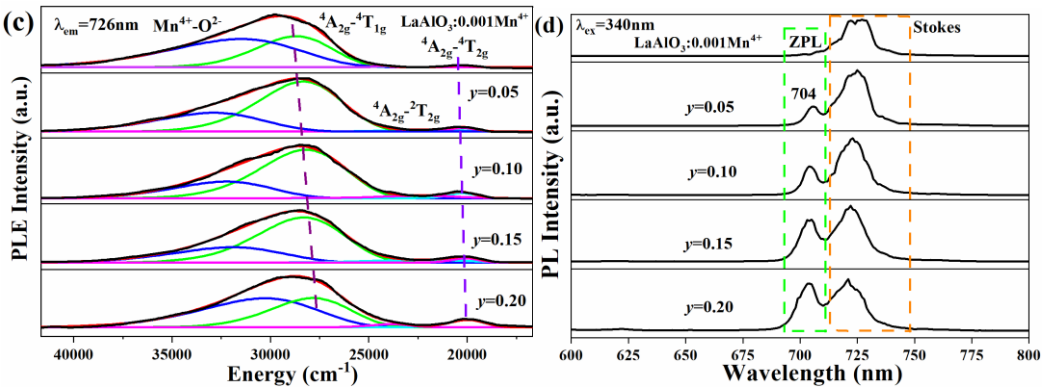

Fig. 7 PLE (a,c) and PL (b,d) spectra for (a,b) LBAT:0.001Mn^{4+} (x=0-0.2) and (c,d) LYAG:0.001Mn^{4+} (y=0-0.2) at 77 K.

Notably, the ZPL emission peak appears by co-doping Ba^{2+}-Ti^{4+} and Y^{3+}-Ga^{3+}, but the positions and the intensities of the ZPL band are significantly different. For $LaAlO_3$:0.001Mn^{4+} sample, the ZPL emission peak is too low to be observed. Based on previous work, the ZPL in $LaAlO_3$:Mn^{4+} is located at ~710 nm.[15] Introducing Ba^{2+}-Ti^{4+} to replace La^{3+}-Al^{3+} results in appearance of the ZPL at 710 nm, which intensity increases slowly with x increase. However, for the LYAG:0.001Mn^{4+} (y=0.05-0.2) phosphors, the position of ZPL is at 704 nm that displays a blue shift compared with that for $LaAlO_3$:Mn^{4+} sample, and the ZPL intensity increases with a further increase in y value. Fig. 8a shows the intensity radio of the ZPL to the total emission. The intensity and energy of the ZPL, which is related to the emission without the participation of any phonons, are only dependent on the host lattice. Compared with the phonon sidebands, ZPL is much more sensitive to the local coordination structure. The intensity is determined by the local symmetry around Mn^{4+}.[32] With the substitution of Ba^{2+}-Ti^{4+} for La^{3+}-Al^{3+}, the local symmetry of Mn^{4+} changes a little due to the competition of the increase of bond distances and the

suppression of octahedral tilting, and, thus, the intensity of ZPL shows a slow increase. However, when co-doping Y^{3+}-Ga^{3+}, owing to the increase of bond distances and octahedral tilting, the local symmetry of Mn^{4+} in LYAG:0.001Mn^{4+} (y=0.05-0.2) decreases gradually, which thus contributes to an enhanced ZPL intensity. In fact, the emission energy of Mn^{4+} corresponds to the hybridization, which is related to Mn-O bond length and O-Mn-O bond angle.[18] Longer Mn-O bond length and larger O-Mn-O bond angle distortion generally lead to a smaller Mn-O hybridization, and then contribute to higher emission energies.[18,19] According to the XRD Rietveld refinement information, LYAG:0.001Mn^{4+} (y=0.05-0.2) samples show shorter Mn-O bond length compared to that for LBAT:0.001Mn^{4+} (x=0.05-0.2), but they exhibit larger O-Mn-O bond angle distortion. Actually, the ZPL emission energies for LYAG:0.001Mn^{4+} samples are higher than those of LBAT:0.001Mn^{4+}. Thus, through considering the influence of two aspects, the results show that octahedral tilting distortion, which affects the serious O-Mn-O bond angle distortion, is more important for the ZPL energy of Mn^{4+} in perovskite oxides.

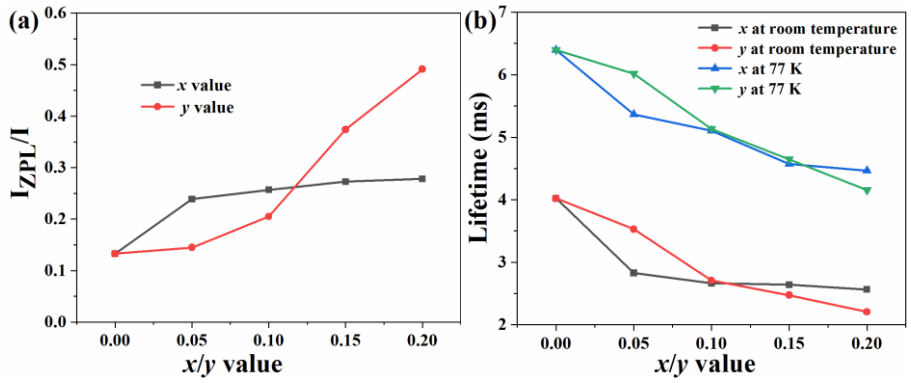

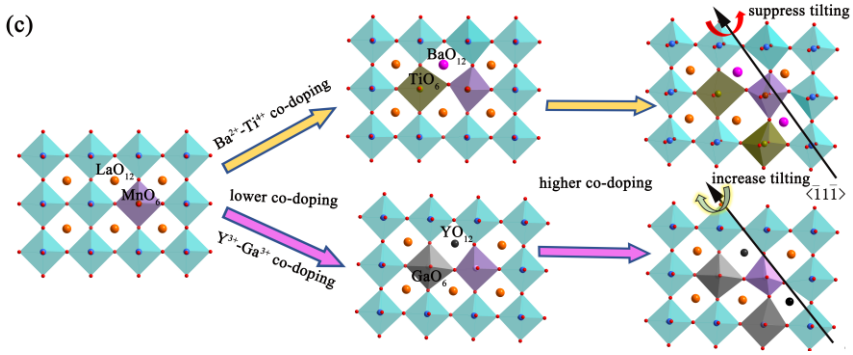

Fig. 8 (a) Related intensity ratio between ZPL and total emission. (b) The variation trend of lifetime at room temperature and 77 K with increasing *x* and *y* value. (c) Structural distortion trend of the MnO_6 octahedron with different doping amounts.

Generally, a long decay time is obtained of luminescence centers in a symmetrical surrounding, while a short decay time is observed when the luminescence centers are located in the distorted site.[33] Figs. S3 and S4 show the fluorescence decay curves corresponding to Mn^{4+} in the LBAT:0.001Mn^{4+} (*x*=0-0.2) and LYAG:0.001Mn^{4+} (*y*=0-0.2) phosphors under the excitation at 340 nm, as monitored at 726 nm at room temperature and at 77 K. All decay curves are found to be well-fitted by a single exponential function, suggesting the single site occupancy of the Mn^{4+} in host lattice. It is expressed as following:[34]

$$I_t = I_0 + Aexp(\frac{-t}{\tau}) \qquad (3)$$

Where I_t and I_0 are the luminescence intensities at time *t* and 0. A refers to a constant and τ represents the exponential component of the decay time. The lifetime decreases with the addition of Ba^{2+}-Ti^{4+} and Y^{3+}-Ga^{3+}. Furthermore, the decrease trend is rapid for LYAG:0.001Mn^{4+} (*y*=0-0.2) phosphors whether at room temperature or at 77 K, compared to that for LBAT:0.001Mn^{4+} (*x*=0-0.2) samples (Fig. 8b). These results are identical with the ZPL intensity variations.

Through above analysis, the energy and intensity of ZPL emission peak is tightly related to the Mn^{4+} local structure environment, as same as the decay time. Fig. 8c shows the structural distortion trend of the MnO_6 octahedron with different doping types and amounts. When Mn^{4+} is incorporated into the $LaAlO_3$ host, Mn^{4+} is surrounded by six coordinated O^{2-} ions to form a MnO_6 octahedron. The MnO_6 octahedron connects with AlO_6 octahedra and LaO_{12} polyhedrons, and Mn^{4+} is located in a high symmetry surrounding environment, leading to a low ZPL intensity and the longest lifetime among all the phosphors. With Ba^{2+}-Ti^{4+} substitution, some O^{2-} vertexes of the MnO_6 octahedron would link to Ba^{2+} and Ti^{4+}, then inducing the change of Mn-O bond length due to the mismatched cation size. However, reducing octahedral tilting also takes place with increasing the *x* value, which makes the MnO_6 be more symmetric. The Mn-O bond lengths and O-M-O bond angles are determined by the two factors. Higher level substitution of Ba^{2+}-Ti^{4+} contributed to a growing number of BaO_{12} and TiO_6 distributed around MnO_6, but the degree of Mn^{4+} symmetry is almost persistent. Thus, the intensity of ZPL increases slowly and the lifetime decrease slowly, owing to the little change of the local symmetry of Mn^{4+}. On the contrary, with the chemical unit co-substitution of Y^{3+}-Ga^{3+} for La^{3+}-Al^{3+}, the distortions are consisted of the cation size mismatch and the increased octahedral tilting. The increased octahedral tilting would make Mn^{4+} to be in a more asymmetrical local environment with increasing the *y* value. Therefore, the ZPL intensity increases quickly and the lifetime decreases linearly with increasing the *y* value. Notably, when a small amount is added, the ZPL intensity for LBAT:0.001Mn^{4+}

(x=0.05, 0.1) is higher than that for LYAG:0.001Mn^{4+} (y=0.05, 0.1) and the lifetime for LBAT:0.001Mn^{4+} (x=0.05, 0.1) is shorter than that for LYAG:0.001Mn^{4+} (y=0.05, 0.1). This is because the average ionic radius of Ba^{2+}-Ti^{4+} is larger than that of Y^{3+}-Ga^{3+} pair, and, so, the distortions arising from cation size mismatch were initially dominant. But the LYAG:0.001Mn^{4+} (y=0.15, 0.2) phosphors show higher ZPL intensity and shorter decay time, compared to LBAT:0.001Mn^{4+} (x=0.15, 0.2) phosphors, because the octahedral tilting takes the dominate role at higher doping contents.

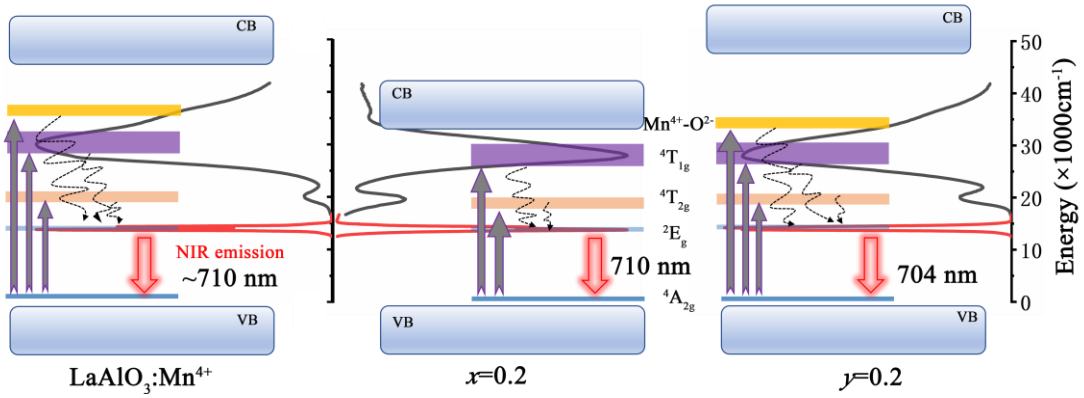

Fig. 9 Mechanisms of luminescence in $LaAlO_3$:0.001Mn^{4+}, x=0.2 and y=0.2 samples.

Fig. 9 displays the mechanisms in $LaAlO_3$:0.001Mn^{4+}, x=0.2 and y=0.2 samples for clear description of the energy transition process. For $LaAlO_3$:0.001Mn^{4+} and y=0.2, the electron is excited from $^4A_{2g}$ energy level to $^4T_{1g}$, $^2T_{2g}$,$^4T_{2g}$ and even the Mn^{4+}-O^{2-} charge-transfer band. However, the observation is different from that for x=0.2 sample. Because the conduction band bottom shifts down and then drowns the Mn^{4+}-O^{2-} level, the excited electron jumps to the conduction band directly, rather than the Mn^{4+}-O^{2-} level. So, the LBAT:0.001Mn^{4+} (x=0.05-0.2) phosphors does not show Mn^{4+}-O^{2-} charge transfer band in excitation spectra. Then, the excited electrons relax

to the ^2E_g level by non-radiative transition process and finally transfer to $^4A_{2g}$ energy level with the output of near-infrared emission. According to the PLE spectra (Figs. 6a and 6c), the samples co-doped by Ba^{2+}-Ti^{4+} and Y^{3+}-Ga^{3+} have lower energy in the $^4T_{1g}$, $^4T_{2g}$ states, which result in red shift of the excitation peak. At the same time, the Stokes and anti-Stokes emissions are kept at same positions, but only the energy of ZPL emission changes, which is clearly described in Fig. 9.

Moreover, the internal quantum yield (IQY) for $LaAlO_3$:0.001Mn^{4+} have been estimated to be 72.5%. For Ba^{2+}-Ti^{4+} co-doping, the IQY of the series LBAT:0.001Mn^{4+} (x=0.05-0.2) phosphors were analyzed to be 66.7% (x=0.05), 62.4% (x=0.1), 59.3% (x=0.15) and 55.8% (x=0.2), respectively. For Y^{3+}-Ga^{3+} co-doping, the IQY of the series LYAG:0.001Mn^{4+} (y=0.05-0.2) were analyzed to be 70.0% (y=0.05), 67.1% (y=0.1), 63.9% (x=0.15) and 61.3% (x=0.2), respectively. The decreased IQY with increasing x or y values is mainly due to the lattice expansion, which induces stronger photon-phonon interaction.[35]

The temperature-dependent luminescence quenching property is essential to evaluate the thermal stability of phosphors.[36-38] The temperature luminescent properties were studied in the temperature range of 298-473 K. Temperature-dependent PL spectra of $LaAlO_3$:0.001Mn^{4+}, x=0.2 and y=0.2 phosphors are demonstrated in Fig. 10a-c. The relative integral emission intensity of the above three samples is plotted in Fig. 10d. The integral intensity of all the samples decreases monotonically. However, the three samples show different degrees of luminescence quenching with increasing the temperature. For better understanding of the thermal

quenching behavior, the Arrhenius equation is used to estimate the activation energy (E_a):[39]

$$I_t = \frac{I_0}{1 + A\exp\left(-\frac{E_a}{kT}\right)} \qquad (4)$$

Where I_0 and I_t are the emission intensities at the initial temperature and working temperature T, respectively. A is a constant and k represents the Boltzmann constant (8.617×10^{-5} eV/K). Linear fitting is conducted and the slope is the value of E_a (Fig. S5). The values are ~0.598, ~0.498 and ~0.583 eV for the $LaAlO_3$:0.001Mn^{4+}, x=0.2 and y=0.2 samples, falling into the range of the reported values of Mn^{4+} doped oxides.[16]

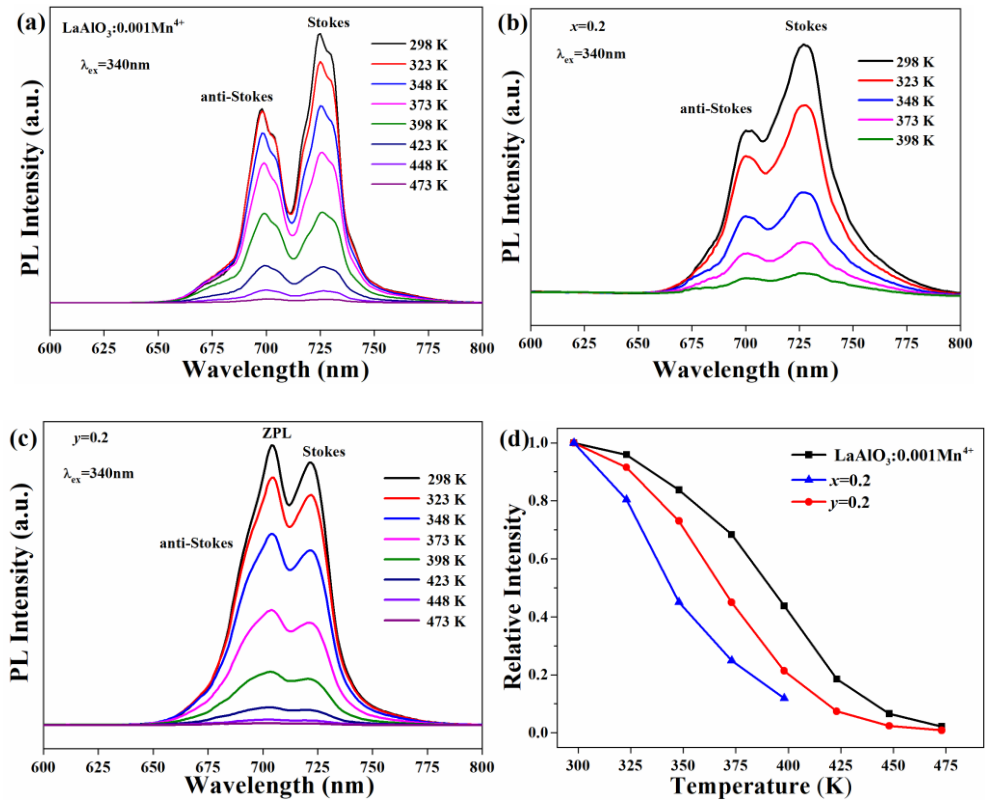

Fig. 10 Temperature-dependent PL spectra of (a) $LaAlO_3$:0.001Mn^{4+}, (b) x=0.2 and (c) y=0.2 phosphors. (d) The relative integrated intensity of the three samples.

4. Conclusion

A series of $La_{1-x}Ba_xAl_{1-x}Ti_xO_3$:0.001$Mn^{4+}$ (LBAT:0.001Mn^{4+}, x=0-0.25) and $La_{1-y}Y_yAl_{1-y}Ga_yO_3$:0.001$Mn^{4+}$ (LYAG:0.001Mn^{4+}, y=0-0.25) samples were successfully synthesized. The substitution of Ba^{2+}-Ti^{4+} and Y^{3+}-Ga^{3+} for La^{3+}-Al^{3+} contributed to the increase of lattice constant and M-O bond length. Furthermore, co-doping Ba^{2+}-Ti^{4+} resulted in the suppression of octahedral tilting. However, more serious octahedral tilting was found for the Y^{3+}-Ga^{3+} substitution. Thus, the distortions of LBAT:0.001Mn^{4+}(x=0.05-0.2) samples are caused by the competition between the mismatched ionic radii and the suppression of octahedral tilting. On the contrary, the distortions of LYAG:0.001Mn^{4+} (x=0.05-0.2) are composed of the mismatched ionic radii and the increased octahedral tilting. The distortions have a significant influence on the Mn^{4+} luminescence. Longer Mn-O bond length induces weaker excitation energy through decreasing D_q for LBAT:0.001Mn^{4+} and LYAG:0.001Mn^{4+} phosphors. But the various D_q could not change the position of emission peak. In fact, the emission shape and energy, particularly the ZPL emission, exhibited big changes by co-doping Ba^{2+}-Ti^{4+} and Y^{3+}-Ga^{3+}. The ZPL intensity increases with substituting Ba^{2+}-Ti^{4+} and Y^{3+}-Ga^{3+} for La^{3+}-Al^{3+}. Because the symmetry around Mn^{4+} decreases slower by co-doping Ba^{2+}-Ti^{4+} than that by co-doping Y^{3+}-Ga^{3+}, the intensity of ZPL for LBAT:0.001Mn^{4+} increases slower than that in LYAG:0.001Mn^{4+}. At the same time, the ZPL energy for LBAT:0.001Mn^{4+} is higher than that for LYAG:0.001Mn^{4+}, owing to larger distortion of the O-Mn-O bond angle.

Conflicts of interest

There are no conflicts to declare.

Acknowledgements

This work was supported in part by the Natural Science Foundation of Liaoning Province (Grant 2020-MS-081), and National Natural Science Foundation of China (Grant 51302032, 51972047, 52172112).

References

1 Y. N. Zheng, R. Z. Zhang, L. Zhang, Q. F. Gu and Z.-A. Qiao, A resol-assisted cationic coordinative co-assembly approach to mesoporous ABO_3 perovskite oxides with rich oxygen vacancy for enhanced hydrogenation of furfural to furfuryl alcohol, *Angew. Chem. Int. Ed.*, 2021, **60**, 4774-4781.

2 J. F. Zhao, J. C. Gao, W. M. Li, Y. T. Qian, X. D. Shen, X. Wang, X. Shen, Z.W. Hu, C. Dong, Q. Z. Huang, L. P. Cao, Z. Li, J. Zhang, C. W. Ren, L. Duan, Q. Q. Liu, R. C. Yu, Y. Ren, S.-C. Weng, H.-J. Lin, C.-T. Chen, L.-H. Tjeng, Y. Long, Z. Deng, J. L. Zhu, X. C. Wang, H. M. Weng, R. Z. Yu, M. Greenblatt and C. Q. Jin, A combinatory ferroelectric compound bridging simple ABO_3 and A-site-ordered quadruple perovskite, *Nat. Commun.*, 2021, **12**, 747.

3 W. R. Geng, X. W. Guo, Y. L. Zhu, Y. J. Wang, Y. L. Tang, M. J. Han, Y. P. Feng, M. J. Zou, B. Wu, J. Y. Ma, W. T. Hu and X. L. Ma, Oxygen octahedral coupling mediated ferroelectric-antiferroelectric phase transition based on domain wall engineering, *Acta Mater.*, 2020, **198**, 145-152.

4 R. Huang, H.-C. Ding, W.-I. Liang, Y.-C. Gao, X.-D. Tang, Q. He, C.-G. Duan, Z.

Q. Zhu, J. H. Chu, C. A. J. Fisher, T. Hirayama, Y. Ikuhara and Y.-H. Chu, Atomic-scale visualization of polarization pinning and relaxation at coherent $BiFeO_3/LaAlO_3$ interfaces, *Adv. Funct. Mater.*, 2014, **24**, 793-799.

5 W. L. Lu, P. Yang, W. D. Song, G. M. Chow and J. S. Chen, Control of oxygen octahedral rotations and physical properties in $SrRuO_3$ films, *Phys. Rev. B*, 2013, **88**, 214115.

6 H. J. Xiang, M. Guennou, J. Íñiguez, J. Kreisel and L. Bellaiche, Rules and mechanisms governing octahedral tilts in perovskites under pressure, *Phys. Rev. B*, 2017, **96**, 054102.

7 Y. C. Ji, P. Zhang, L. Q. He, D. Wang, H. Y. Luo, K. Otsuka, Y. Z. Wang and X. B. Ren, Tilt strain glass in Sr and Nb co-doped $LaAlO_3$ ceramics, *Acta Mater.*, 2019, **168**, 250-260.

8 A. Biswas, C.-H. Yang, R. Ramesh and Y. H. Jeong, Atomically flat single terminated oxide substrate surfaces, *Prog. Surf. Sci.*, 2017, **92**, 117-141.

9 S. A. Hayward, F. D. Morrison, S. A. T. Redfern, E. K. H. Salje, J. F. Scott, K. S. Knight, S. Tarantino, A. M. Glazer, V. Shuvaeva, P. Daniel, M. Zhang and M. A. Carpenter, Transformation processes in $LaAlO_3$: neutron diffraction, dielectric, thermal, optical, and raman studies, *Phys. Rev. B*, 2005, **72**, 054110.

10 P. Bouvier and J. Kreisel, Pressure-induce phase transition in $LaAlO_3$, *J. Phys.: Condens. Matter*, 2002, **14**, 3981-3991.

11 M. V. Abrashev, A. P. Litvinchuk, M. N. Iliev, R. L. Meng, V. N. Popov, V. G. Ivanov, R. A. Chakalov and C. Thomsen, Comparative study of optical phonons in the

rhombohedrally distorted perovskites $LaAlO_3$ and $LaMnO_3$, Phys. Rev. B, 1999, **59**, 4146-4153.

12 S. Y. Li, Q. Zhu, X. D. Sun and J.-G. Li, Magical polyhedral twist via chemical unit co-substitution in $LaAlO_3:Mn^{4+}$ to greatly enhance the zero phonon line for high-efficiency plant-growth LEDs, *J. Mater. Chem. C*, 2021, **9**, 7163-7173.

13 S. Q. Fang, T. C. Lang, T. Han, J. Y. Wang, J. Y. Yang, S. X. Cao, L. L. Peng, B. T. Liu, A. N. Yakovlev and V. I. Korepanov, Zero-thermal-quenching of Mn^{4+} far-red-emitting in $LaAlO_3$ perovskite phosphor via energy compensation of electrons' traps, *Chem. Eng. J.*, 2020, **389**, 124297.

14 T. Hu, H. Lin, Y. Cheng, Q. M Huang, J. Xu, Y. Gao, J. M. Wang and Y. S. Wang, A highly-distorted octahedron with a C_{2v} group symmetry inducing an ultra-intense zero phonon line in Mn^{4+}-activated oxyfluoride $Na_2WO_2F_4$, *J. Mater. Chem. C*, 2017, **5**, 10524-10532.

15 Y. Li, Y.-Y. Li, K. Sharafudeen, G.-P. Dong, S.-F. Zhou, Z.-J. Ma, M.-Y. Peng and J.-R. Qiu, A strategy for developing near infrared long-persistent phosphors: taking $MAlO_3:Mn^{4+},Ge^{4+}$ (M = La, Gd) as an example, *J. Mater. Chem. C*, 2014, **2**, 2019-2027.

16 S. S. Liang, G. G. Li, P. P. Dang, Y. Wei, H. Z. Lian and J. Lin, Cation substitution induced adjustment on lattice structure and photoluminescence properties of $Mg_{14}Ge_5O_{24}:Mn^{4+}$: optimized emission for W-LED and thermometry applications, *Adv. Optical Mater.*, 2019, **7**, 1900093.

17 M. H. Fang, W. L. Wu, Y. Jin, T. Lesniewski, S. Mahlik, M. Grinberg, M. G. Brik,

A. M. Srivastava, C. Y. Chiang, W. Zhou, D. Jeong, S. H. Kim, G. Leniec, S. M. Kaczmarek, H. S. Sheu and R. S. Liu, Control of luminescence by tuning of crystal symmetry and local structure in Mn^{4+}-activated narrow band fluoride phosphors, *Angew. Chem. Int. Ed.*, 2018, **57**, 1797-1801.

18 M. H. Du, Chemical trends of Mn^{4+} emission in solids, *J. Mater. Chem. C*, 2014, **2**, 2475-2481.

19 K. Saritas, W. M. Ming, M. H. Du and F. A. Reboredo, Excitation energies of localized correlated defects via quantum monte carlo: a case study of Mn^{4+}-doped phosphors, *J. Phys. Chem. Lett.*, 2019, **10**, 67-74.

20. D. Fukuda, Microstructure and photoluminescence properties of Mg-doped $BaTiO_3$:Pr^{3+} phosphors, *J. Am. Ceram. Soc.*, 2007, **90**, 2670-2672.

21. G. Gasparotto, L. Tavares, T. Silva, L. Maia and J. Garvalho, Structural and spectroscopic properties of Eu^{3+} doped $Y_4Al_2O_9$ compounds through a soft chemical process, *J. Lumin.*, 2018, **204**, 513-519.

22 T. Ungár, Microstructural parameters from X-ray diffraction peak broadening, *Scripta Mater.*, 2004, **51**, 777-781.

23 M. S. Cai, T. C. Lang, T. Han, D. Valiev, S. Q. Fang, C. Z. Guo, S. S. He, L. L. Peng, S. X. Cao, B. T. Liu, L. Du, Y. Zhong and E. Polisadova, Novel cyan-green-emitting Bi^{3+}-doped $BaScO_2F$, R^+ (R= Na, K, Rb) perovskite used for achieving full-visible-spectrum LED lighting, *Inorg. Chem.*, 2021, **60**, 15519-15528.

24 S. Hariyani and J. Brgoch, Local structure distortion induced broad band emission in the all-inorganic $BaScO_2F$:Eu^{2+} perovskite, *Chem. Mater.*, 2020, **32**, 6640-6649.

25 J. Q. Chen, C. H. Yang, Y. B. Chen, J. He, Z.-Q. Liu, J. Wang and J. L. Zhang, Local structure modulation induced highly efficient far-red luminescence of $La_{1-x}Lu_xAlO_3:Mn^{4+}$ for plant cultivation, *Inorg. Chem.*, 2019, **58**, 8379-8387.

26 G. X. Li, G. Li, Q. Mao, L. Pei, H. Yu, M. J. Liu, L. Chu and J. S. Zhong, Efficient luminescence lifetime thermometry with enhanced Mn^{4+}-activated $BaLaCa_{1-x}Mg_xSbO_6$ red phosphors, *Chem. Eng. J.*, 2022, **430**, 132923.

27 Z.-Q. Ye, S.-G. Xiao and X.-L. Yang, Up-conversion of $Nd^{3+}/Yb^{3+}/Tm^{3+}$ tri-doped $CaTeO_3$ compound under excitation of 808 nm, *Rare Met.*, 2021, **40**, 1008-1013.

28 L. Ma, Z. G. Xia, V. Atuchin, M. Molokeev, S. Auluck, A. H. Reshak and Q. L. Liu, Enginering oxygen vacancies towards self-activated $BaLuAl_xZn_{4-x}O_{7-(1-x)/2}$ photoluminescent materials: an experimental and theoretical analysis, *Phys. Chem. Chem. Phys.*, 2015, **17**, 31188-31194.

29 V. Atuchin, L. Isaenko, V. Kesler, M. Molokeev, A. Yelisseyev and S. Zhurkov, Exploration on anion ordering, optical properties and electronic structure in $K_3WO_3F_3$ elpasolite, *J. Solid State Chem.*, 2012, **187**, 159-164.

30 H. P. Ji, Z. H. Huang, Z. G. Xia, M. S. Molokeev, X. X. Jiang, Z. S. Lin and V. V. Atuchin, Comparative investigations of the crystal structure and photoluminescence property of eulytite-type $Ba_3Eu(PO_4)_3$ and $Sr_3Eu(PO_4)_3$, *Dalton Trans.*, 2015, **44**, 7679-7686.

31 S. Y. Li, Q. Zhu, J. Q. Xiahou and J.-G. Li, Doping Pb^{2+} in $LaAlO_3$ to generate dual emission centers and an optical storage container for visible and near infrared persistent luminescence, *Dalton Trans.*, 2022, **51**, 1112-1122.

32 Y. Zhou, X. M. Wang, C. P. Wang, T. Zhang, Y. G. Wang, F. Dou and H. Jiao, A strong zero-phonon line red phosphor $BaNbF_7:Mn^{4+}$ for white LEDs, *Inorg. Chem. Front.*, 2020, **7**, 3371-3378.

33 T. S. Sreena, P. P. Rao, A. K. V. Raj and T. R. A. Thara, Exploitation of Eu^{3+} red luminescence through order-disorder structural transitions in lanthanide stannate pyrochlores for warm white LED applications, *Phys. Chem. Chem. Phys.*, 2018, **20**, 24287-24299.

34 Q. Zhou, J. Wan, Y. Y. Zhou, S. Zhang, D. X. Shi, X. L. Xie, H. Q. Pu, Y. Q. Ye and Z. L. Wang, Ultraintense zero-phonon line from a Mn^{4+} red-emitting phosphor for high-quality backlight display applications, *Inorg. Chem.*, 2021, **60**, 19197-19205.

35 J. A. Nelson, E. L. Brant and M. J. Wagner, Nanocrystalline Y_2O_3:Eu phosphors prepared by alkalide reduction, *Chem. Mater.*, 2003, **15**, 688-693.

36 H. P. Ji, Z. H. Huang, Z. G. Xia, M. S. Molokeev, M. Y. Chen, V. V. Atuchin, M. H. Fang, Y. G. Liu and X. W. Wu, Phase Transformation in $Ca_3(PO_4)_2:Eu^{2+}$ via the controlled quenching and increased Eu^{2+} content: identification of new cyan-emitting α-$Ca_3(PO_4)_2:Eu^{2+}$ phosphor, *J. Am. Ceram. Soc.*, 2015, **98**, 3280-3284.

37 Y. Wei, C. C. Lin, Z. W. Quan, M. S. Molokeev, V. V. Atuchin, T.-S. Chan, J. Lin and G. G. Li, Structural evolution induced preferential occupancy of designated cation sites by Eu^{2+} in $M_5(Si_3O_9)_2$ (M= Sr, Ba, Y, Mn) phosphors, *RSC Adv.*, 2016, **6**, 57261-57265.

38 G. G. Li, C. C. Lin, W.-T. Chen, M. S. Molokeev, V. V. Atuchin, C.-Y. Chiang, W. Z. Zhou, C.-W. Wang, W.-H. Li, H.-S. Sheu, T.-S. Chan, C. G. Ma and R. S. Liu,

Photoluminescence tuning via cation substitution in oxonitridosilicate phosphors: DFT calculations, different site occupations, and luminescence mechanisms, *Chem. Mater.*, 2014, **26**, 2991-3001.

39 S. Q. Fang, T. C. Lang, T. Han, M. S. Cai, S. X. Cao, L. L. Peng, B. T. Liu, Y. Zhong, A. N. Yakovlev and V. I. Korepanov, A novel efficient single-phase dual-emission phosphor with high resemblance to the photosynthetic spectrum of chlorophyll A and B, *J. Mater. Chem. C*, 2020, **8**, 6245-6253.